1 **BioRT-Flux-PIHM v1.0: a watershed biogeochemical reactive transport**
2 **model**

3 Wei Zhi[1], Yuning Shi[2], Hang Wen[1], Leila Saberi[3], Gene-Hua Crystal Ng[3], Kayalvizhi
4 Sadayappan[1], Devon Kerins[1], Bryn Stewart[1], Li Li[1,*]

5 [1] Department of Civil and Environmental Engineering, The Pennsylvania State University, State
6 College, PA 16802, USA

7 [2] Department of Ecosystem Science and Management, The Pennsylvania State University, State
8 College, PA 16802, USA

9 [3] Department of Earth and Environmental Sciences, University of Minnesota, Twin Cities, MN
10 55455, USA

11 [*] Correspondence to lili@engr.psu.edu

Abstract

Watersheds are the fundamental Earth surface functioning units that connect the land to aquatic systems. Many watershed-scale models represent hydrological processes but lack the representation of multi-component reactive transport processes. This has limited our capability to understand and predict solute export, water chemistry, and earth system response to changing climate and anthropogenic conditions. Here we present a recently developed BioRT-Flux-PIHM (BioRT hereafter) v1.0, a watershed-scale biogeochemical reactive transport model. The model augments the previously developed RT-Flux-PIHM that integrates land-surface interactions, surface hydrology, and abiotic geochemical reactions. It enables the simulation of 1) shallow and deep water partitioning to represent surface water, shallow soil water, and deeper groundwater; 2) biotic processes including plant uptake, soil respiration, and microbially mediated reactions such as nutrient transformation**.** The reactive transport part of the code has been verified against the widely used reactive transport code CrunchTope. BioRT-Flux-PIHM v1.0 has recently been applied in multiple watersheds under diverse climate, vegetation, and geological conditions. This paper briefly introduces the governing equations and model structure with a focus on new model developments. It also showcases one hydrology example that simulates shallow and deep water interactions, and two biogeochemical examples relevant to nitrate and dissolved organic carbon (DOC). These examples are illustrated in two simulation modes of varying complexity. One is the spatially lumped mode (i.e., two land cells connected by one river segment) that focuses on processes and average behavior of a watershed. Another is the spatially distributed mode (i.e., hundreds of cells) that includes details of topography, land cover, and soil properties. Whereas the spatially lumped mode represents more of averaged properties and processes and temporal variations, the spatially distributed mode can be used to understand the impacts of spatial structure and identify hot spots of biogeochemical reactions.

1. Introduction

Watersheds are the fundamental Earth surface units that receive and process water, mass, and energy (Li, 2019;Li et al., 2020;Hubbard et al., 2018). Watershed processes include land surface interactions that regulate evapotranspiration and discharge, and water partitioning between shallow soil lateral flow going into streams versus downward flow and recharge into the deeper subsurface (Figure 1). Complex biogeochemical interactions occur among soil, water, roots, and microbes along water's flow paths, regulating gas effluxes (e.g., CO_2) and solute export (Fatichi et al., 2019;van der Velde et al., 2010;Grathwohl et al., 2013).

These hydrological and biogeochemical processes determine how Earth surface systems respond to hydroclimatic forcing and human perturbations (van der Velde et al., 2014;Miller et al., 2020;Han et al., 2019). Understanding these processes remains challenging due to the complex process interactions. An example is the concentration-discharge (C-Q) relationships of solutes at stream and river outlets. Similar C-Q relationships have been observed for some solutes across watersheds under diverse geological and climatic conditions (Godsey et al., 2009;Basu et al., 2010;Moatar et al., 2017;Zarnetske et al., 2018;Godsey et al., 2019), whereas different solutes have shown contrasting patterns in the same watershed (Miller et al., 2017;Herndon et al., 2015;Musolff et al., 2015). A general theory that can explain contrasting C-Q observations (e.g., flushing vs. dilution behaviors) under diverse watershed characteristics and external conditions remains elusive. The lack of mechanistic understanding presents major roadblocks to forecasting water quality and earth system dynamics in the future.

One of the outstanding challenges is the lack of modeling tools that mechanistically link hydrological and biogeochemical processes at the watershed scale. Model development has advanced mostly within the disciplinary boundaries of hydrology and biogeochemistry (Li, 2019). Watershed hydrologic models focus on solving for water storage and fluxes (Fatichi et al., 2016). Reactive transport models (RTMs) have traditionally focused on transport and multi-component biogeochemical reactions mostly in groundwater systems with limited interactions with climate and other surficial conditions (Steefel et al., 2015;Li et al., 2017b). Some integration crossing disciplinary boundaries

68   did occur in recent years. For example, SWAT (Soil & Water Assessment Tool) has a
69   version that couples with the groundwater model MODFLOW and the surface water and
70   groundwater quality model in RT3D (Bailey et al., 2017; Ochoa et al., 2020). CATHY
71   (Catchment Hydrology) includes processes of pesticide decay (Gatel et al.,
72   2019;Scudeler et al., 2016). Hydrologiska Byråns Vattenbalansavdelning (HBV) and the
73   Hydrological Predictions for the Environment (HYPE)have modules that simulate
74   processes relevant to nutrients and contaminants (Lindström et al., 2005;Lindström et al.,
75   2010). While these models can simulate processes such leaching of nutrients from
76   agriculture lands (Lindström et al., 2005;Lindström et al., 2010;Bailey et al., 2017), they
77   do not explicitly solve the multi-component reactive transport equations. In other words,
78   reactions are often represented rudimentarily without honoring kinetics and
79   thermodynamics theories in soil biogeochemistry and geochemistry. For example,
80   nutrient leaching is calculated based on empirical equations without explicitly solving
81   reactive transport equations. Reaction rates are represented using first-order decay
82   (Gatel et al., 2019), assuming constant reaction rates that do not change with
83   environmental conditions. Biogeochemical processes however are highly variable with
84   seasonal dynamics and depend on local environments such as substrate availability, soil
85   temperature, and soil moisture (Li et al., 2017a;HARTLEY et al., 2007). These models
86   therefore cannot capture the temporal variations in environmental factors that regulate
87   soil biogeochemical reactions and stream and water chemistry.

88   To fill this model capability need, we augmented the watershed model RT-Flux-
89   PIHM (Bao et al., 2017) into BioRT-Flux-PIHM (BioRT hereafter). Compared to RT-Flux-
90   PIHM, BioRT has two additions. One is the capability of simulating biotic processes
91   including plant uptake of nutrients, soil respiration, and other microbe-mediated redox
92   reactions. Examples include soil respiration that produces CO_2 and dissolved organic
93   carbon (DOC), and nutrient transformation reactions such as nitrification and
94   denitrification. The other is the addition of an optional deeper layer below shallow soil to
95   enable the simulation of interacting deep water and shallow soil water flow (Figure 1).
96   Here the deep water is loosely defined as the water below the soil zone, typically in less
97   weathered, fractured subsurface that harbors relatively old and slow-moving groundwater
98   contributing to streams. It is a fundamental component of the hydrologic cycle and water

99 budget. The groundwater-surface water interactions also modulate land-atmospheric
100 energy exchanges and soil moisture dynamics (Keune et al., 2016). Evidence has been
101 mounting in recent years that deeper water below the shallow soil interacts with streams,
102 introduces water with distinct chemistry, sustains base flow in dry times, and buffers
103 climate variability (Gurdak, 2017;Green, 2016;Taylor et al., 2013). Stream chemistry often
104 reflects distinct chemistry from shallow soil water and deeper groundwater at different
105 time, i.e., the so called Shallow and Deep Hypothesis (Zhi et al., 2019;Zhi and Li,
106 2020;Botter et al., 2020). Including the deep water component thus is essential for
107 understanding mechanisms and predicting dynamics of water quality under changing
108 climate and human conditions.

109   This paper introduces the new developments in BioRT. The paper starts with a
110 brief overview of water and energy related processes. It then introduces governing
111 equations and reaction kinetics used in BioRT, followed by three examples that illustrate
112 the new capabilities. The examples include the surface water and groundwater
113 interactions, nitrate transformation and transport, and the production and export of DOC.
114 The model can be set up in both spatially lumped or spatially explicit modes. The source
115 code and the examples shown here are ~~hosted on~~archived on the Zenodo website
116 (https://doi.org/10.5281/zenodo.3936073) and the GitHub website (https://github.com/Li-
117 Reactive-Water-Group/BioRT-Flux-PIHM).

118

119 **2. Model overview**

120   BioRT-Flux-PIHM integrates three modules (Figure 1). The Flux module is for land-
121 surface processes including surface energy balance, solar radiation, and ET (Shi et al.,
122 2013). The hydrology module PIHM simulates water processes including precipitation,
123 interception, infiltration, recharge, surface runoff, subsurface lateral flow, and deep water
124 flow (Qu and Duffy, 2007). The BioRT module simulates solute transport reactions. The
125 abiotic reactions included in RT-Flux-PIHM (Bao et al., 2017) are mineral dissolution and
126 precipitation, aqueous and surface complexation, and ion exchange reactions. The newly
127 added reactions include plant uptake of nutrients, soil respiration, microbe-mediated
128 redox reactions (e.g., carbon decomposition and nutrient transformation).

129
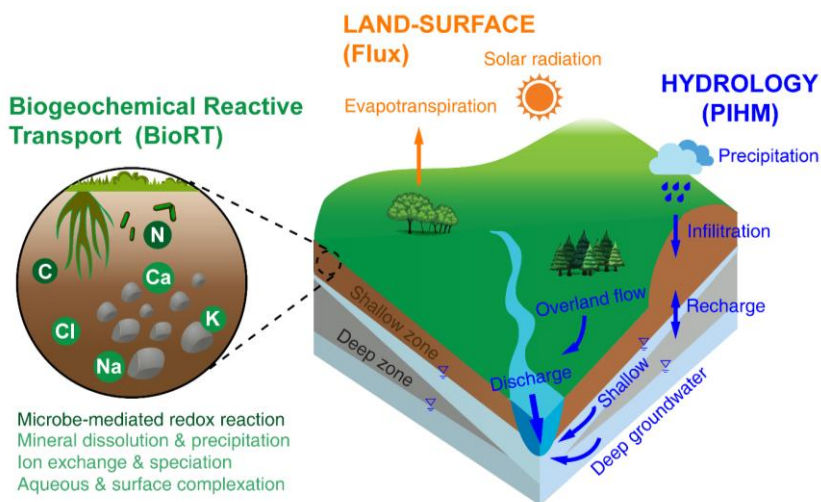
Figure 1. A conceptual diagram for processes at the watershed scale. Land surface interactions include processes such as energy balance, solar radiation, and evapotranspiration; hydrological processes partition water between surface runoff, shallow soil water, and deeper water entering the stream. Soil biogeochemical reactions include abiotic reactions such as weathering (e.g., mineral dissolution and precipitation), ion exchange, surface complexations), and biotic processes such as plant uptake of nutrients, soil respiration, and other microbe-mediated reactions. These processes are represented in three modules: The Flux module for land-surface interactions, the PIHM module for catchment hydrology, and the BioRT module for biogeochemical reactions. Conceptually the shallow zone is the shallow soil and weathered zone that are more conductive to water flow (e.g., soil lateral flow or interflow). The deep zone refers to the less weathered zone that often harbors the old and slow flowing groundwater. Reactions can occur in both shallow and deep zones.

142

The land surface and hydrology modules solve for soil temperature and water storage, from which water fluxes are calculated for surface runoff, shallow and deep water fluxes. The BioRT module uses the calculated soil temperature, water storage, and water fluxes to simulate solute transport (advective and diffusive/dispersive) and biogeochemical reactions in both shallow and deep zones (see governing equations in later sections). The reactions include kinetically controlled (e.g., microbe-mediated redox reaction, mineral dissolution and precipitation) or equilibrium-controlled (e.g., ion exchange, surface complexation (sorption), and aqueous complexation). Users can

151 define the types of reactions to be included and the form of reaction kinetics in input files.
152 The output of BioRT includes the spatial distribution and time series of aqueous and solid
153 concentrations, from which we can infer reaction rates.

154 The model can be set up running in either spatially lumped or spatially explicit
155 modes. When running in spatially explicit mode, the simulation domain can be structured
156 as prismatic grids based on topography. Each grid is partitioned into surface and shallow
157 and deep subsurface layers. The surface layer calculates water flow above ground
158 (surface runoff). The shallow zone is loosely defined as the highly permeable subsurface
159 that contrasts the deep zone that is broadly defined as the lower permeability zone
160 beyond the shallow zone. In many places, the shallow zone is the soil zone that is most
161 conductive to water flow (e.g., lateral flow) and is responsive to hydroclimatic forcing. The
162 deep subsurface zone is the less weathered layer that harbors the old ground water that
163 contributes to stream flow. Note that these definitions differ from those in the hydrology
164 community, which often refers to the shallow soil lateral flow as groundwater, in a way
165 that distinguishes it from the surface runoff (Dingman, 2015). These source waters from
166 different depths of the subsurface often have distinct solid and water chemistry, and are
167 dominant at different hydrological conditions in different time of the year, as have been
168 observed in many catchments and watersheds (Brantley et al., 2018;Zhi et al., 2019;Zhi
169 and Li, 2020;Sullivan et al., 2016). The model is flexible for taking inputs from online data
170 portals or local measurements and it can accommodate low data availability (see the
171 following section of 5 for data need and domain setup).

172

173 **3. Governing equations and processes**

174
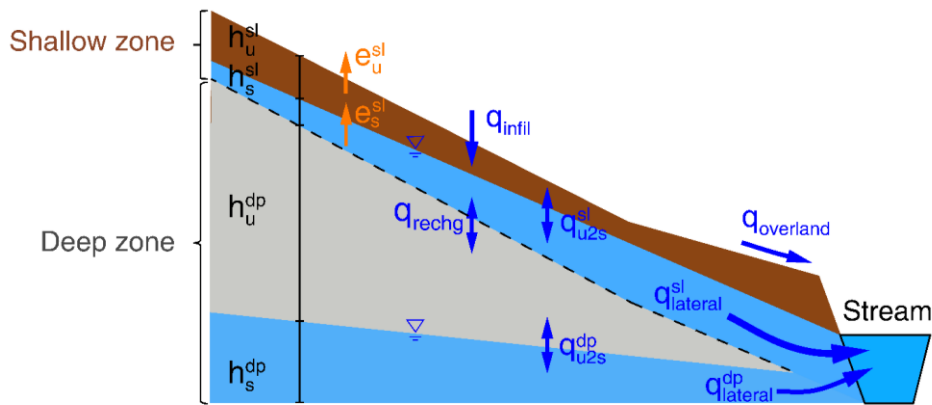
Figure 2. Hillslope view of the shallow and deep zones and relevant water flows. Streams received water primarily from three water flows: the surface runoff ($q_{overland}$), and lateral flow from shallow zone ($q^{sl}_{lateral}$), and the lateral flow that has been recharged and eventually come out from deeper zone ($q^{dp}_{lateral}$). The symbol of "h", "e", and "q" denotes water storage, evapotranspiration, and water flow, respectively. The superscript letter "sl" and "dp" refer to shallow and deep zone, respectively. The subscript letters "u" and "s" refer to unsaturated and saturated layers, respectively. Detailed equations are in section 3.1 – 3.2. The terms "infil", "u2s", and "recharge' refer to infiltration, unsaturated to saturated zones, and recharge.

3.1 Water equations

Flux-PIHM simulates surface runoff and a lumped subsurface flux into streams without distinguishing shallow soil water and deeper groundwater flow paths. Mounting evidence has shown that the shallow soil water and deeper groundwater have distinct chemistry and are dominant at different times of the year (Xiao et al., 2021;Zhi and Li, 2020;Zhi et al., 2019). This means that a lumped subsurface flow cannot describe the dynamics of stream chemistry. We therefore added deeper groundwater zone to simulate deeper water flows that interact with streams. Each prismatic element now has three zones in the vertical direction: surface (or above ground), shallow and deep zones in the subsurface.

In each prismatic element i, the shallow zone includes unsaturated and saturated water storages. The unsaturated zone receives water from the surface via infiltration and flows vertically to the saturated zone. The saturated zone flows both vertically to the deep

197 zone (recharge) and laterally to neighboring grids j or the stream (lateral). The code
198 solves the following equations in the shallow zone:

$$\theta_i^{sl} \frac{dh_{i,u}^{sl}}{dt} = q_{i,inf} - q_{i,u2s}^{sl} - e_{i,u}^{sl} \quad (1)$$

199

$$\theta_i^{sl} \frac{dh_{i,s}^{sl}}{dt} = q_{i,u2s}^{sl} - q_{i,rechg} - e_{i,s}^{sl} + \sum_{1}^{N_{ij}} q_{ij}^{sl} \quad (2)$$

200

201 Where θ_i^{sl} [m³ pore space/m³ total volume] is the shallow zone porosity in element i; $h_{i,u}^{sl}$
202 and $h_{i,s}^{sl}$ [m] are the unsaturated and saturated water storage in the shallow zone,
203 respectively. The storages h here are the height of soil column with equivalent saturated
204 water, not the height of the pure water (100% volume) column. That is why porosity is in
205 the equation. For saturation zones, this height is needed to quantify the depths of water
206 tables and determines the direction of water flow between neighboring grids. The
207 $q_{i,inf}$ [m/s] is the infiltration rate from the surface to the shallow zone; $q_{i,u2s}^{sl}$ [m/s] is the
208 vertical flow from the unsaturated layer to the saturated layer in the shallow zone; $q_{i,rechg}$
209 [m/s] is the recharge rate from the shallow zone to the deep zone; $e_{i,u}^{sl}$ and $e_{i,s}^{sl}$ [m/s] are
210 evapotranspiration (ET) from the unsaturated and saturated layer in the shallow zone,
211 respectively; q_{ij}^{sl} [m/s] are the lateral flows in the shallow saturated layer between the
212 element i and its neighbor element j; N_{ij} (≤ 3) is the number of neighbor elements j. For
213 a prismatic element i, a boundary cell has one or two neighbors; a non-boundary cell has
214 three neighbors. ET is calculated by the Penman potential evaporation scheme (detailed
215 equations in Shi (2012)). A similar set of water equations for the deep zone are in the SI
216 (Eqn. S1 and S2).

217   Infiltration and vertical fluxes from the unsaturated to saturated layer in the shallow
218 zone are based on the Richards equation, in which hydraulic water head H (i.e., the
219 summation of water storage h and elevation head z) and hydraulic conductivity K
220 determine the fluxes:

$$q_{i,inf} = K_{i,inf} \frac{H_{i,sur} - H_{i,u}^{sl}}{d_{i,inf}} \quad (3)$$

221

222
$$q_{i,u2s}^{sl} = K_{i,V}^{sl} \frac{H_{i,u}^{sl} - H_{i,s}^{sl}}{0.5 d_i^{sl}} \quad (4)$$

223 Where $d_{i,inf}$ and d_i^{sl} [m] are the thickness of infiltration layer and shallow zone depth,

224 respectively; $K_{i,inf}$ [m/s] is the hydraulic conductivity of the infiltration layer, the top 0.1 m

225 of the subsurface that has different conductivity from the rest of subsurface; $K_{i,V}^{sl}$ [m/s] is

226 the hydraulic conductivity in the vertical direction (i.e., weighted average of macropore

227 $K_{i,macV}$ and soil matrix $K_{i,satV}$, Eqn. S7); $H_{i,sur}$ [m] is the surface hydraulic water head (=

228 $h_{i,sur} + z_{i,sur}$); $H_{i,u}^{sl}$ and $H_{i,s}^{sl}$ [m] are the shallow hydraulic water heads in the unsaturated

229 and saturated layer, respectively. The lateral flow in the shallow saturated layer is

230 calculated using Darcy's law:

231
$$q_{ij}^{sl} = K_{ij}^{sl} \frac{H_{i,s}^{sl} - H_{j,s}^{sl}}{d_{ij}} \quad (5)$$

232 Where d_{ij} [m] is the distance between the centers of elements i and j; K_{ij}^{sl} [m/s] is the

233 harmonic mean of shallow hydraulic conductivity in the horizontal direction between

234 elements i ($K_{i,H}^{sl}$) and j ($K_{j,H}^{sl}$). The interaction between the shallow saturated zone and

235 stream channel also follows Eqn. 5, except that the adjacent head is replaced by the level

236 of stream water. Similar to the shallow zone, hydrological equations in the deep zone are

237 detailed in the SI (Eqn. S1 – S8).

238

239 **3.2 Reactive transport equations**

240   The governing advection dispersion reaction (ADR) equation for an arbitrary solute

241 m in an element i is as follows (Bao et al., 2017):

242
$$V_i \frac{d(S_{w,i}\theta_i C_{m,i})}{dt} = \sum_1^{N_{ij}} \left(A_{ij} D_{ij} \frac{C_{m,j} - C_{m,i}}{d_{ij}} - q_{ij} A_{ij} C_{m,j} \right) + R_{m,i}, \qquad m = 1, ..., nm \quad (6)$$

243 Where V_i [m³ total volume] is the total volume of element i; $S_{w,i}$ [m³ water/m³ pore space]

244 is soil water saturation; θ_i [m³ pore space/m³ total volume] is the porosity; $C_{m,i}$ [mol/m³

245 water] is the aqueous concentration of species m; N_{ij} is the number of fluxes from

246   neighbor element j for element i, N_{ij} is 2 for the unsaturated zone (infiltration, recharge)

247   with only vertical flows and 5 for saturated zone with flux from (or to) the unsaturated

248   zone, from (or to) the deeper zone, and fluxes between i and three neighbor elements j

249   in lateral flow directions for non-boundary grids; A_{ij} [m^2] is the grid area shared by i and

250   its neighbor grid j; D_{ij} [m^2/s] is the hydrodynamic dispersion coefficient (i.e., sum of

251   mechanical dispersion and effective diffusion coefficient) normal to the shared surface

252   A_{ij}; d_{ij} [m] is the distance between the center of i and its neighbor elements j; q_{ij} [m/s]

253   is the flow rate across A_{ij}; $R_{m,i}$ [mol/s] is the total rate of kinetically controlled reactions in

254   element i that involve species m; nm is the total number of independent primary species

255   to be solved for reactive transport equations. Equation (6) states that the change of solute

256   mass (the left term) is driven by dispersive transport, advective transport, and reactions

257   (i.e., the 1st, 2nd, and 3rd right-hand side terms, respectively).

258

259   **3.3 Biogeochemical processes and reaction kinetics**

260   **3.3.1 Biogeochemical processes**

261   Here we discuss representative biogeochemical processes that involve plants and

262   microbes that can be included in BioRT. BioRT differs from general water quality models

263   that primarily target a few contaminants (e.g., N, P, metals). The framework of BioRT is

264   flexible and the users can define reactions and solutes of interests in the input files. For

265   abiotic reactions such as mineral dissolution and surface complexation or ion exchange,

266   readers are referred to (Bao et al. (2017). Generally speaking, shallow soils contain more

267   weathered materials and soil organic matters (SOM) including roots, leaves, and

268   microbes. SOM can be decomposed partially into organic molecules that dissolve in

269   water, i.e., Dissolved Organic Carbon (DOC). It can also become oxidized completely

270   into CO_2, which can emit back to the atmosphere in gas form (Davidson, 2006) or

271   transport and enter streams in the form of dissolved inorganic carbon (DIC). With

272   coexisting cations (e.g., Ca, Mg), DIC can precipitate out and become carbonate minerals

273   (e.g., $CaCO_3$).

274
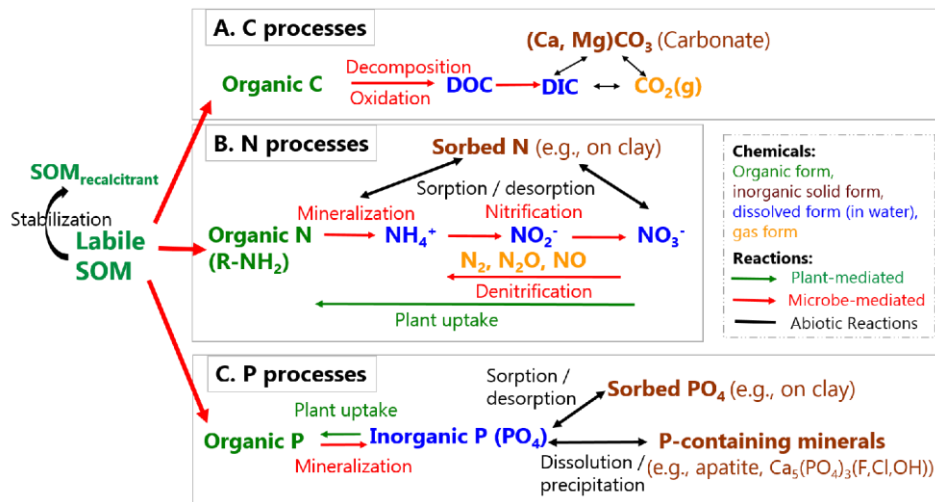
Figure 3. Biotic and abiotic reactions relevant to the transformation of soil organic matter (SOM).
SOM can become stabilized (recalcitrant) through sorption on clay and separation from reactants.
Labile OM can decompose into inorganic forms, releasing C, N, and P that further transform into
various forms (adopted from Li (2019), permission with Mineralogical Society of America).

OM decomposition releases organic nitrogen (R-NH$_2$), which can further react to
become NH$_4^+$ and other nitrogen forms (N$_2$, N$_2$O, NO, NO$_2^-$, NO$_2$) (Figure 3). The gases
can emit back to the atmosphere. Denitrification requires anoxic conditions and occurs
less commonly in shallow soils owing to the pervasive presence of O$_2$ (Sebestyen et al.,
2019); denitrification can become important under wet conditions and in O$_2$-depleted
groundwater aquifers. Phosphorous (P) can be in organic forms in organic matter, sorbed
on fine soil particles, dissolved in water, or in solid forms as P-containing minerals.
Transformation of nutrients occurs through various bio-mediated or abiotic reactions. A
representative P-containing mineral in the Earth´s crust is apatite Ca$_5$(PO$_4$)$_3$(F, Cl, OH).
Once liberated via rock dissolution, P is biologically assimilated and locked in organic
forms. These organic forms have very low solubility, allowing them to bind on and be
transported together with soil particles in the form of orthophosphate or pyro-diphosphate.

3.3.2 Reaction kinetics in natural soils

294 **Rate dependence on temperature and soil moisture.** Reactions such as soil
295 respiration and plant uptake typically depend on environmental conditions (temperature
296 or soil moisture). For example, in shallow oxic soils where organic carbon and O_2 are
297 often abundant, the rate law for carbon decomposition can be simplified to the following
298 form assuming microorganism concentrations are relatively constant.

299 $$r = kAf(T)f(S_w)f(Z_w) \quad (7)$$

300 Where the reaction rate r [mol/s] depends on rate constant k [mol/m²/s], the surface area
301 A [m²] is a lumped parameter that quantitatively represents SOM content and biomass
302 abundance, $f(T)$ and $f(S_w)$ describe the temperature and soil moisture dependence,
303 respectively, $f(Z_w)$ can be included to account for the depth distribution of SOM (Seibert
304 et al., 2009), and Z_w [m] is the water table depth. An example for the depth distribution is
305 $f(Z_w) = \exp\left(-\frac{Z_w}{b_m}\right)$ (Weiler and McDonnell, 2006;Bai et al., 2016), with b_m as the depth
306 coefficient describing the gradient of SOM content over depth. Users can choose to
307 include either one or all of these dependencies in input or database files.

308 The temperature dependence follows a Q_{10}-based form (Lloyd and Taylor,
309 1994;Friedlingstein et al., 2006;Hararuk et al., 2015) as follows:

310 $$f(T) = Q_{10}^{(T-20)/10} \quad (8),$$

311 where Q_{10} is the relative increase in reaction rates when temperature increases by 10 °C
312 (Davidson and Janssens, 2006). Values of Q_{10} (Figure 4a) can vary from 1.0 to 3.0,
313 depending on climatic conditions, substrate availability, and ecosystem type (e.g.,
314 grassland, forest) (Davidson et al., 2006;Liu et al., 2017). The mean values are in the
315 range of 1.4 to 2.5 (Zhou et al., 2009;Bracho et al., 2016). The Q_{10} value can be specified
316 in the input file.

317 The soil moisture dependence function $f(S_w)$ is coded in the following form:

318
$$
\begin{cases}
(\frac{S_w}{S_{w,c}})^n, S_w \le S_{w,c} \\
(\frac{1 - S_w}{1 - S_{w,c}})^n, S_w > S_{w,c}
\end{cases}
\quad (9)
$$

319 Here $S_{w,c}$ [0 to 1] is the critical soil moisture at which rates are highest, and n is the
320 exponent reflecting the dependence of rates on soil moisture. A typical n value is 2 (Yan
321 et al., 2018) with a range between 1.2 and 3.0 (Hamamoto et al., 2010), depending on
322 soil structure and texture. As shown in Figure 4b, the form indicates an intermediate
323 critical soil moisture $S_{w,c}$ at which $f(S_w)$ reaches its maximum. When $S_w \leq S_{w,c}$, $f(S_w)$
324 increases with S_w; when $S_w > S_{w,c}$, $f(S_w)$ decreases with S_w (Figure 4b) (Yan et al.,
325 2018). Under the extreme conditions of $S_{w,c}$ equals to 0 or 1, $f(S_w)$ monotonically
326 increase or decrease (Figure 4c). The two parameters, $S_{w,c}$ and n, determines the shape
327 of the curve. They can be specified in input or database files. One can also choose not to
328 have temperature or soil moisture dependence by choosing parameters that would lead
329 to the value of exponent being zero.
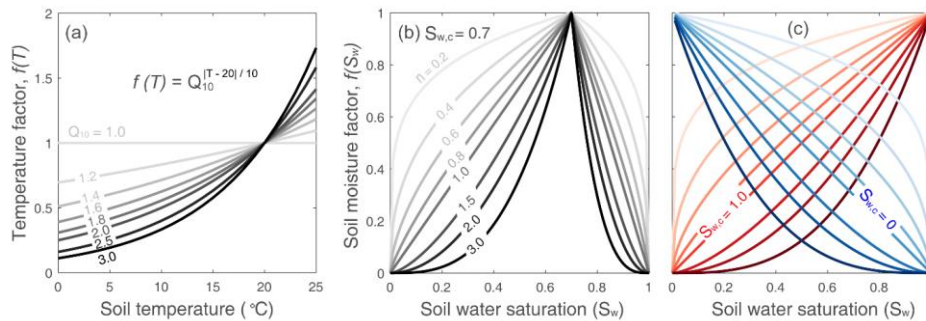
330
331 **Figure 4**. Reaction rate dependence. (a) Function form of soil temperature dependence and (b,
332 c) soil moisture dependence for reaction rates. The $f(T)$ takes Q_{10} form (Equation 8). The soil
333 moisture factor $f(S_w)$ depends on $S_{w,c}$ and n and soil water saturation S_w (Equation 9). The soil
334 moisture function can represent three types of behaviors: the threshold behavior (b, $0 < S_{w,c} < 1$),
335 increase behavior (red in (c), $S_{w,c} = 1$), and decrease behavior (blue in (c), $S_{w,c} = 0$). Values of n
336 = 1 leads to a linear threshold dependence of S_w while $n < 1$ and $n > 1$ lead to concave and
337 convex dependences, respectively.

338

339 **Rate dependence on substrates: Monod kinetics and biogeochemical redox**
340 **ladder.** Deeper groundwater aquifers often experience anoxic conditions that lead to
341 processes such as denitrification or methanogenesis. This can also happen in wetlands
342 or wet soils. Under such conditions, the rates of microbe-mediated redox reactions
343 depend not only on temperature and soil moisture as discussed above, they also depend

344 on concentrations of electron donors and non-oxygen electron acceptors (e.g., nitrate,
345 iron oxides, sulfate) that are often limited under anoxic conditions (Bao et al., 2014;Li,
346 2019;Benettin et al., 2020). The order of redox reactions typically follows the
347 biogeochemical redox ladder, which is based on how much microbe can harvest energy
348 by reducing different types of electron acceptors. Monod reaction rate laws are often used
349 for quantifying rates of these redox conditions. These rate laws are detailed in the section
350 S2 of Supporting Information. Users can combine these Monod rate laws and the
351 temperature and soil moisture dependence described above, if needed.
352

3.4 Plant related processes: root uptake of nitrate as an example

354 Nutrient uptake by plants is complex and remains poorly understood. A variety of
355 plant uptake models exists with varying degrees of complexity (Neitsch et al., 2011;Fisher
356 et al., 2010;Cai et al., 2016). These models are mostly based on plant growth module or
357 supply and demand approach that often requires detailed phenological and plant
358 attributes including growth cycle, root age and biomass, nutrient availability, and carbon
359 allocation, in addition to local temperature and soil moisture (Neitsch et al.,
360 2011;Porporato et al., 2003;Dunbabin et al., 2002;Buysse et al., 1996;Fisher et al., 2010).
361 Without detailed mechanistic understanding, we assume a simple and operational
362 approach. In the Example 2 that we show later, for example, nitrate uptake was modelled
363 with dependence on NO_3^- concentration, soil temperature and moisture, and rooting
364 density (McMurtrie et al., 2012;Yan et al., 2012;Buljovcic and Engels, 2001).

$$r_{uptake} = k_{uptake} C_{NO_3^-} f(T) f(S_w) f_{root}(d_w) \quad (13)$$

$$f_{root}(d_w) = \exp((-d_w + \delta)/\lambda) \quad (14)$$

367 Where k_{uptake} [L/s] is the nitrate uptake rate, $f_{root}(d_w)$ is the normalized rooting density
368 term in the range of 0 to 1 as a function of water depth to the groundwater (d_w). The
369 rooting term (Eqn. 14) was exponentially fitted ($\delta = 0.013, \lambda = 0.20$) based on field
370 measurements of root distribution along depth (Hasenmueller et al., 2017). It is common
371 to observe root density decrease exponentially in forests (López et al., 2001). Other form
372 of user-tailored plant uptake rate law can be added if needed.

373

4. Numerical scheme and model verification

The system of differential equations for water storages (e.g., Eqn. 1 and 2, and Eqn. S1 and S2) are assembled into a global system of ordinary differential equations (ODEs). It issolved in CVODE (short for C-language Variable-coefficients ODE solver, https://computing.llnl.gov/projects/sundials/cvode), a numerical ODE solver in the SUite of Nonlinear and Differential / ALgebraic equation Solvers (SUNDIALS) (Hindmarsh et al., 2005). In BioRT, the transport step is first solved with water by the preconditioned Krylov (iterative) method and the Generalized Minimal Residual Method (Saad and Schultz, 1986). All primary species in in element I are then assembled in a local matrix and solved iteratively using the Crank-Nicolson and Newton-Raphson methods in CVODE (Bao et al., 2017).

Model verification. The BioRT module had been verified against CrunchTope under different transport and reaction conditions (Figures S1 – S7 in SI). CrunchTope is a widely used subsurface reactive transport model (Steefel and Lasaga, 1994;Steefel et al., 2015), and is often used as a benchmark to verify other reactive transport models. Verification was performed under simplified hydrological conditions with 1-D column and constant flow rates such that it focuses on advection, diffusion, dispersion, and biogeochemical reactions. Specifically, three cases were verified. The phosphorus case that involves kinetics-controlled apatite dissolution and thermodynamics-controlled phosphorous speciation was first tested for solution accuracy of the bulk code that was inherited from the original RT-Flux-PIHM. Soil carbon and nitrogen processes were further verified for solution accuracy of the augmented BioRT module. Table S7 shows an average percent bias and Nash Sutcliffe efficiency (NSE) of 1.1% and 0.98, indicating a robust performance for a variety of solutes under different transport and reaction conditions. Note NSE ranges from $-\infty$ to 1, with NSE = 1 being the perfect fit (Moriasi et al., 2007).

5. Model structure, data needs, and domain setup

Model structure. The model takes meteorological forcing time series as input and solves for water storages and soil temperature, along with other hydrologic and land

surface states and fluxes (Figure 5). BioRT reads in the model output of water and temperature from Flux-PIHM, and solves the biogeochemical reactive transport equations. At the time scale of months to years that are typical for BioRT simulations, alterations in solid phase properties, including, porosity, permeability, and reactive surface area, are considered negligible such that hydrological parameters remain constant with time.

Data needs. The code sets up the model domain based on watershed characteristics including topography, land cover, and shallow and deep zone properties (Figure 5). When the model is used in a spatially distributed form, the model domain is set up using elevation, land cover, soil and geology maps supplied by the user. A useful data portal is the Geospatial Data Gateway (https://datagateway.nrcs.usda.gov). Another geospatial data source is the HydroTerre (http://www.hydroterre.psu.edu/), where users can obtain data on elevation, land cover, geology, and soil (Leonard and Duffy, 2013). Meteorological forcing data can be downloaded from the North American Land Data Assimilation Systems Phase 2 (NLDAS-2, https://ldas.gsfc.nasa.gov/nldas/v2/forcing). The vegetation forcing, i.e., Leaf Area Index (LAI), can be obtained from MODIS (Moderate Resolution Imaging Spectroradiometer, https://modis.gsfc.nasa.gov/data). Other vegetation properties (e.g., shading fraction, rooting depth) can be adopted from, for example, the Noah vegetation parameter table embedded in the Weather Research and Forecasting model (WRF; Skamarock and Klemp (2019)). Local measurements from meteorological stations and field campaigns (e.g., land cover, soil, geology) can be used in the model. Initial water and solid phase chemistry can be based on measurements or general knowledge of the simulated sites. The form of reaction rate laws can be defined in the input files and calibrated to reproduce field data. Reaction thermodynamics, mostly equilibrium constants, are from the geochemical database EQ3/6 by default (Wolery, 1992). These reaction parameters can be modified when necessary. The model outputs include aqueous and solid concentrations of shallow and deep zone and stream water.

431
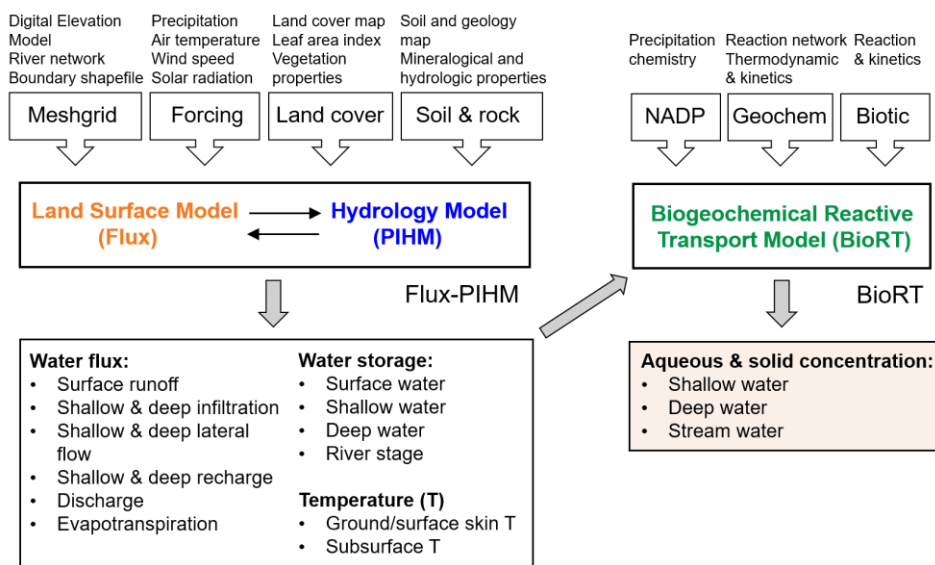
Figure 5. Model structure, input, and output of BioRT-Flux-PIHM. The Flux-PIHM takes in watershed characteristics including topography (digital elevation model, DEM), land cover, shallow and deep zone properties, and meteorological forcing time series and solves for water storage, and ground and soil temperature. BioRT takes in water- and temperature-related output from Flux-PIHM and additional inputs such as precipitation chemistry and shallow and deep water chemistry and biogeochemical kinetics parameters, and solve for aqueous and solid concentrations in the shallow and deep zone, and stream water. NADP stands for the National Atmospheric Deposition Program.

Domain set up: from simple, spatially lumped to complex, spatially distributed domains. The domain can be set up at different spatial resolutions with different numbers of grids. A simple domain can be set up with two land grids representing two sides of a watershed connected by one river cell. This setup uses averaged properties without needs for larger spatial data. Alternatively, a complex domain can be set up to track "hot spots" of biogeochemical reactions using many grids with explicit representation of spatial details (e.g., topographic map, river network, land use map, soil and geology map, mineral distribution). The model domain can be set up using PIHM-GIS (http://www.pihm.psu.edu/pihmgis_home.html), a standalone GIS interface for watershed delineation, domain decomposition, and parameter assignment (Bhatt et al., 2014). The

same processes (e.g., hydrology, reaction network) can be setup in both types of spatial configurations. Auto-calibration is not built into the model, but a global calibration coefficient approach is used to reduce parameter dimension and facilitate manual calibration. A typical model application requires 20 to 30 hydrological parameters to be calibrated. These parameters include land surface parameters (e.g., canopy resistance, surface albedo), soil and geology parameters (e.g., hydraulic conductivity, porosity, Van Genuchten, macropore properties) (Shi et al., 2013). Reaction-related parameters (e.g., reaction rate constant, mineral surface area, Q_{10}, $S_{w,c}$, and n) are additionally needed for calibration, the number of which depends on the numbers of reactions involved in a particular system.

6. Model applications

The original RT-Flux-PIHM has been applied to understand processes related to the geogenic solutes of Cl and Mg at the Shale Hills watershed and for Na in a watershed on Volcán Chimborazo in the Ecuadorian Andes (Table 1). The new BioRT-Flux-PIHM has been demonstrated for understanding the dynamics of DOC and nitrate at Shale Hills and Coal Creek. This section will present one hydrology and two biogeochemical examples in the Susquehanna Shale Hills Critical Zone Observatory (SSHCZO), a small headwater watershed in central Pennsylvania, USA. The mean annual precipitation is approximately 1,070 mm and the mean annual temperature is 10°C (Brantley et al., 2018). Soil carbon storage and respiration and nitrogen budget and fluxes have been studied in detail (Andrews et al., 2011;Hasenmueller et al., 2015;Weitzman and Kaye, 2018). Modeling work has been conducted to understand hydrological dynamics (Shi et al., 2013;Xiao et al., 2019), transport of the non-reactive tracer Cl, and the weathering-derived solute Mg (Bao et al., 2017;Li et al., 2017a).

Table 1. Example Model applications of BioRT-Flux-PIHM

Watershed (location)	Size (km^2)	Model domain	Modeled solutes	Reactions (rate laws: 1, TST; 2, Monod based; 3, plant uptake)	Reference

		Spatially distributed	Cl, Mg	• Chlorite dissolution[1] • Illite dissolution[1] • Cation exchange	Bao et al., 2017; Li et al., 2017
Shale Hills (PA, USA)	0.08	Spatially distributed	DOC	• SOC decomposition[2] • DOC sorption	Wen et al., 2020
		Spatially lumped	NO_3^-	• Soil N leaching[2] • Denitrification[2] • Plant uptake[3]	This work
Coal Creek (CO, USA)	53	Spatially lumped	DOC, Na	• SOC decomposition[2] • DOC sorption • Albite dissolution[1]	Zhi et al., 2019
Volcán Chimborazo (Ecuador)		Spatially distributed	Cl, Na, Ca, Mg, SiO_2	• Albite dissolution[1] • Diopside dissolution[1]	Saberi et al. (2021)

Note: Transition State Theory (TST) is a classic kinetic rate law for mineral dissolution and precipitation (Brantley et al., 2008) (Eqn. S15); . SOC stands for soil organic carbon.

6.1 Example 1: Shallow and deep water interactions

The model was set up using the spatially lumped mode with two grids and one river grid characterized by average land cover, soil and rock properties based on previous work. The model assumed the dominant soil type (Weikert soil) at Shale Hills. The porosity of the deep zone was set to a tenth of the shallow soil porosity based on measurements of the groundwater aquifer (Brantley et al., 2018;Kuntz et al., 2011). In a headwater catchment like Shale Hills where the deep groundwater is most likely sourced from recharge, the deep groundwater contribution to the stream can be primarily controlled by the hydraulic conductivity (K_{satH}) contrast between the deep and shallow zones (i.e., K_{satH}^{dp} / K_{satH}^{sl}). This is because the K_{satH} contrast determines the partitioning of infiltrating water between the shallow lateral flow and the downward recharge to the deep zone and then deep groundwater flow. Two cases of high (red) and low (blue) K_{satH}^{dp} were set up to showcase the control of K_{satH} contrast on deep groundwater (Figure 6a). By changing the deep zone K_{satH}^{dp} from 2.6 to 0.22 (m/d), the annual deep groundwater (Q_G) contribution to discharge (Q) decreased from 26% to 5.2%, although the total stream discharge remains the same. This indicates that the changing K_{satH}^{dp} mostly changes the flow partitioning between the shallow soil flow and deeper groundwater flow into streams.

497
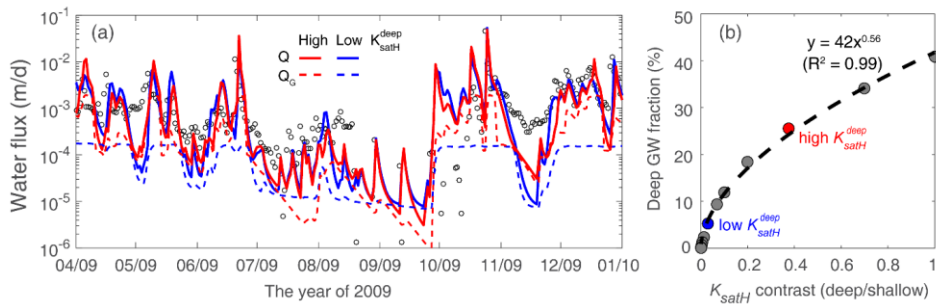
Figure 6. (a) Hydraulic conductivity (K_{satH}) contrast controls the proportion of deep groundwater (Q$_G$). The cases of high ($K_{satH}^{dp} = 2.6\ m/d$, red) and low conductivity ($K_{satH}^{dp} = 0.22\ m/d$, blue) led to 26% and 5.2% of annual Q$_G$ contribution to discharge (Q), respectively. (b) Deep groundwater fraction as a function of K_{satH} contrast between the deep and shallow zone. The upper limit of the deep / shallow K_{satH} contrast was set to 1 as most watersheds have smaller K_{satH} in the deep zone than in the shallow zone. The two red and blue dots correspond to the two cases in left panel.

Several additional cases were further tested to examine the relationship between deep groundwater fraction (%) of discharge and K_{satH} contrast. Figure 6b shows that the deep groundwater fraction rapidly increases with the increasing ratio of K_{satH}^{dp} / K_{satH}^{sl}, reaching a limit when K_{satH} contrast is sufficiently high. The deep groundwater contribution to the stream reaches ~ 40% when K_{satH}^{dp} and K_{satH}^{sl} are equal. In natural systems, we do see places, for example, karst formations, where groundwater contributes to more than 40% (Hartmann et al., 2014;Husic, 2018). These places may have higher deeper conductivity than shallow soils due to the development of highly conductive conduits.

6.2 Example 2: Nitrate dynamics in a spatially implicit domain

This example focuses on nitrate (NO$_3^-$), a dominant dissolved N form in water (https://criticalzone.org/shale-hills/data/datasets/) (Weitzman and Kaye, 2018). The N processes at Shale Hills include atmospheric N deposition, soil N leaching, stream export, denitrification, and plant uptake (Figure 7). Based on field measurements, the atmospheric deposition at the site is the dominant N input; N export via discharge is only

522   a small fraction (2.5%) of atmospheric N input. Most deposited N is tightly cycled by plants
523   or lost to the atmosphere via denitrification.
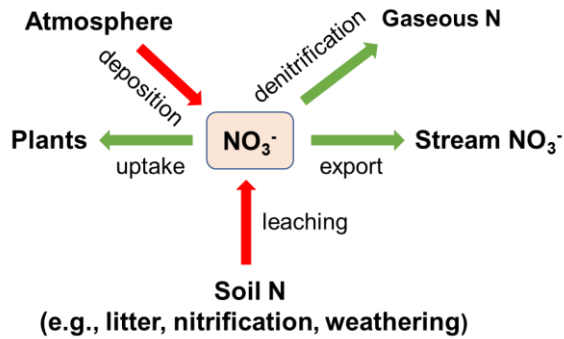
524
525   **Figure 7.** Modeled nitrogen processes in Example 2. Atmospheric N deposition is the major N
526   input; denitrification and plant uptake are the major N loss and sink. Export via discharge only
527   occupies a small fraction.
528

529   The soil N leaching process was represented using a lumped reaction that
530   generates NO_3^-. Conceptually this could represent the total rates of reactions including
531   the decomposition of soil organic matter (SOM), nitrification, and rock weathering that
532   generates NO_3^-. Its rate was assumed to depend on soil temperature and moisture and
533   follows the equation $r_{leach} = kAf(T)f(S_w)$, where r_{leach} [mol/s] is the leaching rate, $k =$
534   $10^{-9.7}$ [mol/m^2/s] is the leaching rate constant (Regnier and Steefel, 1999), and A [m^2] is
535   the surface area that represents the contact area between substrates and N transforming
536   microbe, and $f(T)$ and $f(S_w)$ are soil temperature (Eqn. 8) and soil moisture (Eqn. 9)
537   functions, respectively. The surface area was calculated based on SOM volume fraction
538   [m^3/m^3], specific surface area (SSA, [m^2/g]), substrate density [g/cm^3], and element
539   volume [m^3].

540   Denitrification converts NO_3^- to N_2 gas under anaerobic conditions. Here this
541   process was modeled by the Monod rate law with DOC as the electron donor (Di Capua
542   et al., 2019), NO_3^- as the electron acceptor, and with an inhibition term $f(O_2)$ (Eqn. S13).
543   The reaction rate: $r_{denitrification} = kA \frac{C_{DOC}}{K_{m,DOC}+C_{DOC}} \frac{C_{NO_3^-}}{K_{m,NO_3^-}+C_{NO_3^-}} f(O_2)f(T)f(S_w)$, where $k =$
544   10^{-10} [mol/m^2/s] is the denitrification rate constant (Regnier and Steefel, 1999), half-

545   saturation constants $K_{m,DOC} = 15\,[uM]$ and $K_{m,NO_3^-} = 45\,[uM]$ (Regnier and Steefel,

546   1999). For soil N leaching and denitrification, the SSA were respectively tuned as 1.6 ×

547   10^{-6} and 7.5×10^{-5} [m^2/g] to reproduce observed stream nitrate dynamics. The calibrated

548   values were orders of magnitude lower than the lab measured SSA of natural materials

549   (e.g., SOM, 0.6 ~ 2 m^2/g) (Rutherford et al., 1992). Such discrepancies between

550   calibrated effective reactive surface area (i.e., solid-water contact area) and lab measured

551   absolute surface area are consistent with other observations in literature (Li et al.,

552   2014;Heidari et al., 2017;Wen and Li, 2017, 2018). The uptake rate constant was

553   calibrated by constraining the partitioning of N transformation flux between denitrification

554   and plant uptake by the ratio of 1:5, a value estimated from field measurements of

555   gaseous N outputs (3.53 kg-N/ha/yr) and plant N uptake (18.3 kg-N/ha/yr) (Weitzman and

556   Kaye, 2018). The uptake rate constant in the deep zone (> 2 m in depth) was considered

557   negligible (Hasenmueller et al., 2017). Groundwater nitrate was initialized as 0.43 mg/L,

558   the average of measured groundwater concentration during 2009 - 2010.

559

560   **Temporal nitrate dynamics.** Three cases were set up to understand and quantify the

561   effects of different processes in determining nitrate dynamics (Figure 8a). The *transport-*

562   *only* case (dashed line, *tran*) simulates nitrate input from precipitation (at 1.4 ± 0.96 mg/L,

563   based on the 2009 data of NADP PA42 site) and N transport but without any reactions. It

564   overestimated stream nitrate data (0.33 ± 0.39 mg/L) throughout the year. The *transport*

565   *+ N reactions* case (gray line, *tran + N react*) has denitrification and soil N leaching

566   processes but not plant uptake. These two reactions lowered the nitrate concentration

567   slightly, as these two processes compensate each other in adding and removing nitrate

568   from water. The *transport + N reactions + uptake* case (thick black line, *tran + N react +*

569   *upta)* have all processes. It significantly lowered the nitrate concentration, especially in

570   April-May and October-December. Nitrate peaks from May to July, exhibiting comparable

571   levels of high nitrate concentration (Figure 8b). It is noticeable that the three cases almost

572   overlapped at these overestimated short nitrate peaks, suggesting nitrate-rich

573   precipitation may not be routed into the subsurface where denitrification and plant uptake

574   could occur.

575   Although precipitation from April to August accounted for 70% of the total
576 simulation period, larger storm events in October contributed more to nitrate export.
577 Deeper groundwater had higher nitrate concentration than shallow water, because most
578 plant uptake occurred in the shallow zone. The nitrate fluxes into the deeper zone
579 however only contributed 26% of stream nitrate export at the annual scale, due to the
580 relatively small groundwater contribution (9.5%) to the stream. Denitrification and plant
581 uptake largely occurred during wet spring with leaves growing. Denitrification peaks often
582 appeared after major storm events because wet conditions facilitate denitrification.
583 Comparing the three outfluxes (Figure 8c), nitrate export via discharge (red) was
584 negligible compared to denitrification (blue) and plant uptake (green). At the annual scale,
585 stream export accounted for 9.5%, whereas denitrification and plant uptake took up 15%
586 and 75% of deposited NO_3^-, respectively. In other words, as Nitrate enters this system via
587 precipitation, plant uptake can play a significant role in reducing nitrate level, indicating
588 precipitated nitrate is tightly cycled in the system.
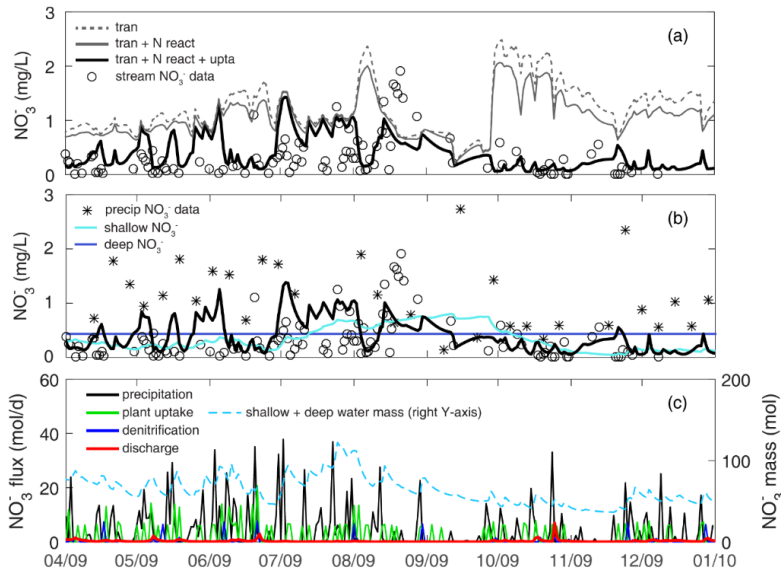
589

590 **Figure 8.** Stream nitrate dynamics and fluxes at Shale Hills in Example 2. (a) Three simulation
591 scenarios with different processes are demonstrated here: *transport-only* (dashed line, *tran*),
592 *transport + N reaction* (gray line, *tran + N react*), *transport + N reaction + plant uptake* (thick black

593 line, *tran + N react + upta*), where N reactions include both nitrate leaching and denitrification (see
594 Figure 7); (b) nitrate concentration in precipitation, shallow and deep water; (c) nitrate fluxes and
595 budget. Note that nitrate leaching was ignored in (b) due to its minimal flux as N deposition from
596 rainfall was the dominant input (Weitzman and Kaye, 2018).

597

598 **6.3 Example 3: DOC production and export in a spatially distributed domain**

599   This example showcases the application of BioRT-Flux-PIHM in a spatially
600 distributed mode. This work has been documented with full details in Wen et al. (2020).
601 Here we only introduce some key features and capabilities in the spatially distributed
602 mode. The Shale Hills catchment was discretized into 535 prismatic land elements and
603 20 stream segments through PIHMgis based on the topography (Figure 9a). The
604 heterogeneous distributions of soil depth and solid organic carbon within the domain
605 (Figure 9b-c) were interpolated through ordinary kriging based on field surveys (Andrews
606 et al., 2011;Lin, 2006). Other soil and mineralogy properties such as hydraulic
607 conductivity, van Genuchten parameters, and ion exchange capacity were spatially
608 distributed following intensive field measurements (Jin and Brantley, 2011;Jin et al., 2010)
609 (criticalzone.org/shale-hills/data/).

610
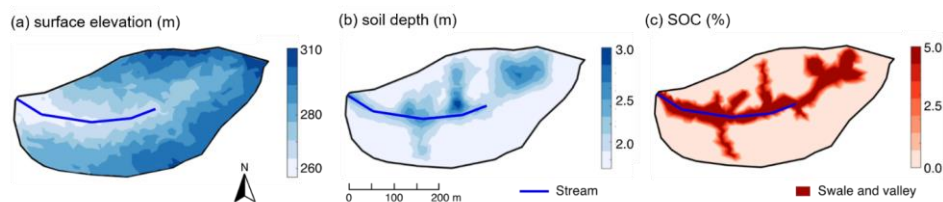
611 **Figure 9**. Attributes of Shale Hills in the spatially distributed mode in Example 3: (a) surface
612 elevation, (b) soil depth, and (c) soil organic carbon (SOC). The surface elevation was generated
613 from lidar topographic data (criticalzone.org/shale-hills/data); Soil depths and SOC were
614 interpolated using ordinary kriging based on field surveys (Andrews et al., 2011;Lin, 2006). The
615 SOC distribution in (c) was further simplified using the high, uniform SOC (5% v/v) in swales and
616 valley soils based on field survey (Andrews et al., 2011). Swales and valley floor areas were
617 defined based on surface elevation via field survey and a 10 m resolution digital elevation model
618 (Lin, 2006).

619

620 **Temporal and spatial patterns of DOC production and export.** The model outputs
621 followed the general trend of stream DOC measurements with the model evaluation index

622 NSE of 0.55 for monthly DOC concentration (Figure 10a). NSE ~~ranges from −∞ to 1.0~~
623 ~~(i.e., perfect fit) with~~ values greater than 0.5 are considered good performance for monthly
624 water quality model (Moriasi et al., 2015). The model reproduced high DOC values (~15
625 mg/L) in the dry periods (July-September). The model enabled the identification of
626 reaction hot spots. In May when soil water is relatively abundant, the valley and swales
627 with deeper soils (Figure 10b) are generally wetter compared to the hillslope and ridgetop,
628 and are hydrologically connected to the stream (Figure 10b, c). The distribution of local
629 DOC production rate r_{DOC} and DOC concentration followed that of SOC (Figure 10c) and
630 water content (Figure 10b). Low r_{DOC} in relatively dry planar hillslopes and uplands
631 resulted in low soil water DOC. The average stream DOC (~5 mg/L) reflected soil water
632 DOC in the valley and swales.

633   In August, the hydrologically-connected zones with high water content shrank to
634 the vicinity of the stream and river bed. With high temperature in summer, r_{DOC} increased
635 by 2-fold from May across the whole catchment while still exhibited the highest values in
636 the SOC-rich regions. Soil water DOC concentration increased by a factor of 2 because
637 the produced DOC was trapped in low soil moisture areas that were not hydrologically
638 connected to the stream. In the north side with low water content (Figure 10b), the soil
639 water DOC (~7 mg/L in average) accumulated more than the south side (~5 mg/L in
640 average). The high shallow water DOC (~10 mg/L) in the stream vicinity dominated the
641 stream DOC in August.

642   In October, precipitation wetted the catchment again. The hydrologically
643 connected zones expanded beyond swales and the valley to the upland hillslopes (Figure
644 10c). The increase in hydrological connectivity zones favored the mixing of shallow water
645 DOC sourced from upland hillslopes (low DOC), swales, and valley (high DOC) into
646 stream rather than only from the stream vicinity with high DOC in the dry August, leading
647 to a drop in stream DOC.

(a) temporal DOC dynamics at the stream outlet

May (wet)   August (dry)   October (wet after dry)

(b) soil moisture

(c) hydrological connected zones

(d) local DOC production rate r_{DOC}

(e) shallow water DOC

648
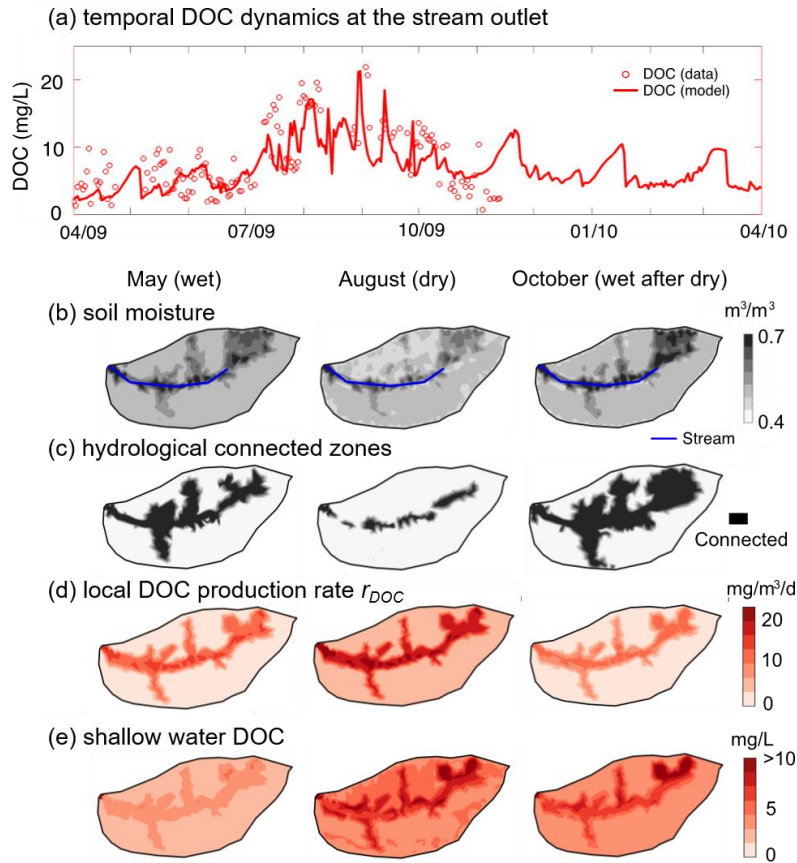
Figure 10. (a) Temporal dynamics of stream DOC concentration; spatial profiles of (b) shallow
soil moisture, (c) hydrologically connected zones, (d) local DOC production rates r_{DOC} and (e)
shallow water DOC concentration in May (wet), August (dry), and October (wet after dry) of 2009.
The soil DOC and r_{DOC} were high in swales and valley with relatively high shallow water and SOC
content. August had the highest shallow water DOC concentration compared to May and October,
because most DOC accumulated in zones that are disconnected to the stream.

C-Q patterns. The DOC C-Q relationship showed a non-typical pattern with flushing first
and transitioning into a dilution pattern, with an overall C-Q slope b = -0.23 (Figure 11).
At low discharges (< 1.8×10^{-4} m/d) in the summer dry period, the stream DOC mainly
came from the organic-rich swales and valley floor zones with high soil water DOC (Figure

660   10e). With discharge increasing in wetter period (i.e., spring and fall), the contribution
661   from planar hillslopes and uplands with lower DOC concentration increased (Figure 10e),
662   leading to the dilution of stream DOC.
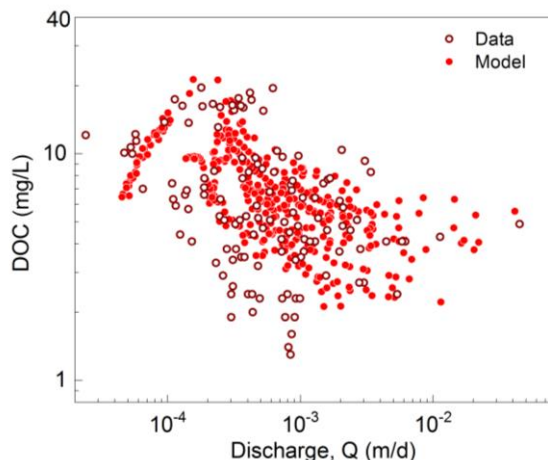
663

664   **Figure 11**. Relationships between daily discharge (Q) and stream DOC concentration. With the
665   increasing Q, the stream water first shifted from the dominance of groundwater with low DOC at
666   very low discharge to the predominance of organic-rich soil water from swales and valley at
667   intermediate discharge. As the discharge increases further, the stream water switches to the
668   dominance of high flow with lower DOC water from planar hillslopes and uplands, resulting in a
669   dilution C-Q pattern (modified from Wen et al., 2020).

670

671   **7. Discussion**

672   BioRT-Flux-PIHM brings the reactive transport modeling capabilities to the
673   watershed scale, enabling the simulation of subsurface shallow and deep flow paths and
674   biogeochemical reactions influenced by hydroclimatic conditions and land-surface
675   interactions. The expanded model capability of simulating bio-mediated processes such
676   as plant uptake, soil respiration, and microbe-mediated redox reactions enables the
677   simulation of carbon and nutrient cycling in the shallow subsurface. The inclusion of the
678   deep groundwater zone allows the exploration of the effects of subsurface structure on
679   hydrological partitioning between shallow soil lateral flow and deep groundwater, and their
680   relationships with stream discharge. Although not shown here, the model can also
681   simulate deeper groundwater coming from regional aquifers across the outer boundary.

This can be particularly useful for watersheds of higher stream orders, where a large proportion of deep water may come from nearby regional aquifers.

The advantage and disadvantages of simple versus complex models have long been debated in the modeling community (Fatichi et al., 2016;Li et al., 2020;Wen et al., 2021). The computational cost of solving a spatially distributed, nonlinear, multi-component reactive transport model is high, posing challenges for the application of ensemble-based analysis. With additional reactions and transport processes, the model includes more functions (such as reaction kinetic rate laws) and parameters (e.g., reaction rate constants, surface area) than hydrological models. The complexity brings in issues of equifinality, uncertainty, and data demands (Beven, 2001, 2006;Kirchner et al., 1996). These issues will persist even though reactive transport models will be constrained by additional chemical data.

It is in this spirit of balancing the cost and gain that we present both spatial distributed and lumped modes for the BioRT model (Li et al., 2020). Compared to the distributed version, the spatially implicit model requires less spatial data and is computationally inexpensive. It can assess the average dynamics of water and solute dynamics and focus on the interacting processes without resolving spatial details. The lumped approach can accommodate basins with low data availability, and it can be easier for students to learn. In contrast, spatially explicit representations enable the exploration of the "hot spots" (e.g., swales and riparian zones with high soil water DOC concentrations in Figure 10e) and their contribution to stream chemistry at different times. Spatial heterogeneities in watershed properties (e.g., soil types and depth, lithology, vegetation, biomass, and mineralogy) are ubiquitous in natural systems and are challenging to resolve. A general understanding of the linkage between local catchment features and catchment-scale dynamics (e.g., stream concentration dynamics and solute export pattern) is often lacking. The spatially distributed model provides a tool to explore these questions. Ultimately, the choice of the model complexity level depends on research questions that the model is set to answer and the available data. At the end, we all need to balance cost and gain when deciding to use a simple or complex model, striving to be "simple but not simplistic" (Beven and Lane, 2019).

8. Summary and conclusion

712

713   This paper introduces the watershed-scale biogeochemical reactive transport code

714 BioRT (short for BioRT-Flux-PIHM). The code integrates processes of land-surface

715 interactions, surface hydrology, and multi-component biogeochemical reactive transport.

716 The new development enables the simulation of 1) biotic reactions including plant uptake,

717 soil respiration, and microbe-mediated redox reactions, and 2) surface water interactions

718 with groundwater from deeper subsurface that still interacts with streams. BioRT has been

719 verified against the widely used reactive transport code CrunchTope for soil carbon,

720 nitrogen, and phosphorus processes. It has been applied to understand carbon, nitrogen,

721 and weathering processes at Shale Hills in Pennsylvania, Coal Creek in Colorado, and

722 Volcán Chimborazo watershed in Andes in Ecuador. Here we showcase the modeling

723 capability of surface-groundwater interactions and reactive transport processes relevant

724 to nitrate and DOC in Shale Hills in two simulation modes. One is in a spatially lumped

725 mode using averaged properties and another is in a spatially distributed mode with

726 consideration of spatial heterogeneity. Results show that the deep groundwater flow that

727 interacts with the stream is primarily controlled by the hydraulic conductivity contrast

728 between shallow and deep zone. biogeochemical reactions in shallow soil primarily

729 determine the stream water chemistry under high flow conditions. The spatially lumped

730 method with two lumped grids can capture the temporal dynamics of average behavior

731 and mass balance; the spatially distributed running mode can be used to understand the

732 spatial dynamics and to identify "hot spots" of reactions. The code can be used for

733 biogeochemical reactive transport simulations in watersheds under diverse climate, land

734 cover, and geology conditions.

735

736 **Data availability**. Field data (e.g., discharge, stream chemistry) is archived at Shale Hills

737 data portal: http://criticalzone.org/shale-hills/data/datasets/ or maintained at HydroShare:

738 https://www.hydroshare.org/group/147.

739

740 **Code availability**. The current model release (BioRT-Flux-PIHM v1.0) is archived at:

741 https://doi.org/10.5281/zenodo.3936073. Documentation, source code, and examples

742 are available at GitHub repository: https://github.com/Li-Reactive-Water-Group/BioRT-

743 Flux-PIHM.

744

Competing interests. The authors declare that they have no conflict of interest.

746

Author contributions. LL conceived the model idea and oversaw the model development. WZ coded the BioRT module, verified the code against the benchmark reactive transport model CrunchTope, and applied and tested the model at Shale Hills watershed. YS developed the deep groundwater component and integrated the BioRT-Flux-PIHM v1.0 into the MM-PIHM family. WH, LS, KS, DK, BS, and GHCN tested the code during its development and contributed study cases.

753

Acknowledgement. We acknowledge the funding support from the Department of Energy, Subsurface Biogeochemistry Program DE-SC0020146, National Science Foundation Hydrological Sciences EAR-1758795. LS and GCN were supported by National Science Foundation Grant EAR-1759071. We appreciate data from the Susquehanna Shale Hills Critical Zone Observatory (SSHCZO) supported by National Science Foundation Grant EAR – 0725019 (C. Duffy), EAR – 1239285 (S. Brantley), and EAR – 1331726 (S. Brantley). Data were collected in Penn State's Stone Valley Forest, which is funded by the Penn State College of Agriculture Sciences, Department of Ecosystem Science and Management, and managed by the staff of the Forestlands Management Office.

References

Andrews, D. M., Lin, H., Zhu, Q., Jin, L., and Brantley, S. L.: Hot spots and hot moments of dissolved organic carbon export and soil organic carbon storage in the Shale Hills catchment, Vadose Zone Journal, 10, 943-954, 2011.

Bai, J., Zhang, G., Zhao, Q., Lu, Q., Jia, J., Cui, B., and Liu, X.: Depth-distribution patterns and control of soil organic carbon in coastal salt marshes with different plant covers, Sci Rep-Uk, 6, 34835, 10.1038/srep34835, 2016.

Bailey, R., Rathjens, H., Bieger, K., Chaubey, I., and Arnold, J.: SWATMOD-Prep: Graphical User Interface for Preparing Coupled SWAT-MODFLOW Simulations, JAWRA Journal of the American Water Resources Association, 53, 400-410, https://doi.org/10.1111/1752-1688.12502, 2017.

Bao, C., Wu, H., Li, L., Newcomer, D., Long, P. E., and Williams, K. H.: Uranium Bioreduction Rates across Scales: Biogeochemical Hot Moments and Hot Spots during a Biostimulation Experiment at Rifle, Colorado, Environmental Science & Technology, 48, 10116-10127, 10.1021/es501060d, 2014.

Bao, C., Li, L., Shi, Y., and Duffy, C.: Understanding watershed hydrogeochemistry: 1. Development of RT‐Flux‐PIHM, Water Resources Research, 53, 2328-2345, 2017.

Basu, N. B., Destouni, G., Jawitz, J. W., Thompson, S. E., Loukinova, N. V., Darracq, A., Zanardo, S., Yaeger, M., Sivapalan, M., Rinaldo, A., and Rao, P. S. C.: Nutrient loads exported from managed catchments reveal emergent biogeochemical stationarity, Geophys. Res. Lett., 37, 10.1029/2010GL045168, 2010.

Benettin, P., Fovet, O., and Li, L.: Nitrate removal and young stream water fractions at the catchment scale, Hydrological Processes, 34, 2725-2738, https://doi.org/10.1002/hyp.13781, 2020.

Beven, K.: How far can we go in distributed hydrological modelling?, Hydrol. Earth Syst. Sci., 5, 1-12, 10.5194/hess-5-1-2001, 2001.

Beven, K.: A manifesto for the equifinality thesis, Journal of Hydrology, 320, 18-36, 10.1016/j.jhydrol.2005.07.007, 2006.

Beven, K., and Lane, S.: Invalidation of Models and Fitness-for-Purpose: A Rejectionist Approach, in: Computer Simulation Validation: Fundamental Concepts, Methodological Frameworks, and Philosophical Perspectives, edited by: Beisbart, C., and Saam, N. J., Springer International Publishing, Cham, 145-171, 2019.

Bhatt, G., Kumar, M., and Duffy, C. J.: A tightly coupled GIS and distributed hydrologic modeling framework, Environmental Modelling & Software, 62, 70-84, http://dx.doi.org/10.1016/j.envsoft.2014.08.003, 2014.

Botter, M., Li, L., Hartmann, J., Burlando, P., and Fatichi, S.: Depth of Solute Generation Is a Dominant Control on Concentration-Discharge Relations, Water Resources Research, 56, e2019WR026695, https://doi.org/10.1029/2019WR026695, 2020.

Bracho, R., Natali, S., Pegoraro, E., Crummer, K. G., Schädel, C., Celis, G., Hale, L., Wu, L., Yin, H., and Tiedje, J. M.: Temperature sensitivity of organic matter decomposition of permafrost-region soils during laboratory incubations, Soil Biology and Biochemistry, 97, 1-14, 2016.

Brantley, S. L., Kubicki, J. D., and White, A. F.: Kinetics of water-rock interaction, 2008.

Brantley, S. L., White, T., West, N., Williams, J. Z., Forsythe, B., Shapich, D., Kaye, J., Lin, H., Shi, Y. N., Kaye, M., Herndon, E., Davis, K. J., He, Y., Eissenstat, D., Weitzman, J., DiBiase, R., Li, L., Reed, W., Brubaker, K., and Gu, X.: Susquehanna Shale Hills Critical Zone Observatory: Shale Hills in the Context of Shaver's Creek Watershed, Vadose Zone Journal, 17, 1-19, ARTN 180092

10.2136/vzj2018.04.0092, 2018.

Buljovcic, Z., and Engels, C.: Nitrate uptake ability by maize roots during and after drought stress, Plant and Soil, 229, 125-135, 2001.

809   Buysse, J., Smolders, E., and Merckx, R.: Modelling the uptake of nitrate by a growing plant with an
810   adjustable root nitrate uptake capacity, Plant and Soil, 181, 19-23, 1996.
811   Cai, X., Yang, Z.-L., Fisher, J., Zhang, X., Barlage, M., and Chen, F.: Integration of nitrogen dynamics into
812   the Noah-MP land surface model v1. 1 for climate and environmental predictions, Geoscientific Model
813   Development (Online), 9, 2016.
814   Davidson, E. A., and Janssens, I. A.: Temperature sensitivity of soil carbon decomposition and feedbacks
815   to climate change, Nature, 440, 165-173, 10.1038/nature04514, 2006.
816   Davidson, E. A., Janssens, I. A., and Luo, Y.: On the variability of respiration in terrestrial ecosystems:
817   moving beyond Q10, Global Change Biology, 12, 154-164, 2006.
818   Davidson, E. A., Janssens, I.A.: Temperature sensitivity of soil carbon decomposition and feedbacks to
819   climate change, Nature, 440, 165-173, 2006.
820   Di Capua, F., Pirozzi, F., Lens, P. N. L., and Esposito, G.: Electron donors for autotrophic denitrification,
821   Chemical Engineering Journal, 362, 922-937, https://doi.org/10.1016/j.cej.2019.01.069, 2019.
822   Dingman, S. L.: Physical hydrology, Waveland press, 2015.
823   Dunbabin, V. M., Diggle, A. J., Rengel, Z., and Van Hugten, R.: Modelling the interactions between water
824   and nutrient uptake and root growth, Plant and Soil, 239, 19-38, 2002.
825   Fatichi, S., Vivoni, E. R., Ogden, F. L., Ivanov, V. Y., Mirus, B., Gochis, D., Downer, C. W., Camporese, M.,
826   Davison, J. H., and Ebel, B.: An overview of current applications, challenges, and future trends in
827   distributed process-based models in hydrology, Journal of Hydrology, 537, 45-60, 2016.
828   Fatichi, S., Manzoni, S., Or, D., and Paschalis, A.: A Mechanistic Model of Microbially Mediated Soil
829   Biogeochemical Processes: A Reality Check, Global Biogeochemical Cycles, 33, 620-648,
830   10.1029/2018gb006077, 2019.
831   Fisher, J., Sitch, S., Malhi, Y., Fisher, R., Huntingford, C., and Tan, S. Y.: Carbon cost of plant nitrogen
832   acquisition: A mechanistic, globally applicable model of plant nitrogen uptake, retranslocation, and
833   fixation, Global Biogeochemical Cycles, 24, 2010.
834   Friedlingstein, P., Cox, P., Betts, R., Bopp, L., von Bloh, W., Brovkin, V., Cadule, P., Doney, S., Eby, M., and
835   Fung, I.: Climate–carbon cycle feedback analysis: results from the C4MIP model intercomparison, Journal
836   of climate, 19, 3337-3353, 2006.
837   Gatel, L., Lauvernet, C., Carluer, N., Weill, S., Tournebize, J., and Paniconi, C.: Global evaluation and
838   sensitivity analysis of a physically based flow and reactive transport model on a laboratory experiment,
839   Environmental Modelling & Software, 113, 73-83, https://doi.org/10.1016/j.envsoft.2018.12.006, 2019.
840   Godsey, S. E., Kirchner, J. W., and Clow, D. W.: Concentration–discharge relationships reflect chemostatic
841   characteristics of US catchments, Hydrol. Process., 23, 1844-1864, 10.1002/hyp.7315, 2009.
842   Godsey, S. E., Hartmann, J., and Kirchner, J. W.: Catchment chemostasis revisited: Water quality responds
843   differently to variations in weather and climate, Hydrological Processes, 33, 3056-3069,
844   https://doi.org/10.1002/hyp.13554, 2019.
845   Grathwohl, P., Rügner, H., Wöhling, T., Osenbrück, K., Schwientek, M., Gayler, S., Wollschläger, U., Selle,
846   B., Pause, M., and Delfs, J.-O.: Catchments as reactors: a comprehensive approach for water fluxes and
847   solute turnover, Environmental earth sciences, 69, 317-333, 2013.
848   Green, T. R.: Linking climate change and groundwater, in: Integrated groundwater management, Springer,
849   Cham, 97-141, 2016.
850   Gurdak, J. J.: Groundwater: Climate-induced pumping, Nature Geoscience, 10, 71, 2017.
851   Hamamoto, S., Moldrup, P., Kawamoto, K., and Komatsu, T.: Excluded‐volume expansion of Archie's law
852   for gas and solute diffusivities and electrical and thermal conductivities in variably saturated porous
853   media, Water Resources Research, 46, 2010.
854   Han, B., Benner, S. G., and Flores, A. N.: Including Variability across Climate Change Projections in
855   Assessing Impacts on Water Resources in an Intensively Managed Landscape, Water, 11, 286, 2019.

856 Hararuk, O., Smith, M. J., and Luo, Y.: Microbial models with data-driven parameters predict stronger soil
857 carbon responses to climate change, Glob. Chang. Biol., 21, 2439-2453, 10.1111/gcb.12827, 2015.
858 HARTLEY, I. P., HEINEMEYER, A., and INESON, P.: Effects of three years of soil warming and shading on the
859 rate of soil respiration: substrate availability and not thermal acclimation mediates observed response,
860 Global Change Biology, 13, 1761-1770, https://doi.org/10.1111/j.1365-2486.2007.01373.x, 2007.
861 Hartmann, J., Lauerwald, R., and Moosdorf, N.: A brief overview of the GLObal RIver CHemistry Database,
862 GLORICH, Procedia Earth and Planetary Science, 10, 23-27, 2014.
863 Hasenmueller, E. A., Jin, L., Stinchcomb, G. E., Lin, H., Brantley, S. L., and Kaye, J. P.: Topographic controls
864 on the depth distribution of soil CO_2 in a small temperate watershed, Applied Geochemistry, 63, 58-69,
865 2015.
866 Hasenmueller, E. A., Gu, X., Weitzman, J. N., Adams, T. S., Stinchcomb, G. E., Eissenstat, D. M., Drohan, P.
867 J., Brantley, S. L., and Kaye, J. P.: Weathering of rock to regolith: The activity of deep roots in bedrock
868 fractures, Geoderma, 300, 11-31, 2017.
869 Heidari, P., Li, L., Jin, L., Williams, J. Z., and Brantley, S. L.: A reactive transport model for Marcellus shale
870 weathering, Geochimica et Cosmochimica Acta, 217, 421-440, 2017.
871 Herndon, E. M., Dere, A. L., Sullivan, P. L., Norris, D., Reynolds, B., and Brantley, S. L.: Landscape
872 heterogeneity drives contrasting concentration–discharge relationships in shale headwater catchments,
873 Hydrology and earth system sciences, 19, 3333-3347, 2015.
874 Hindmarsh, A. C., Brown, P. N., Grant, K. E., Lee, S. L., Serban, R., Shumaker, D. E., and Woodward, C. S.:
875 SUNDIALS: Suite of nonlinear and differential/algebraic equation solvers, ACM Transactions on
876 Mathematical Software (TOMS), 31, 363-396, 2005.
877 Hubbard, S. S., Williams, K. H., Agarwal, D., Banfield, J., Beller, H., Bouskill, N., Brodie, E., Carroll, R.,
878 Dafflon, B., and Dwivedi, D.: The East River, Colorado, Watershed: A mountainous community testbed for
879 improving predictive understanding of multiscale hydrological–biogeochemical dynamics, Vadose Zone
880 Journal, 17, 2018.
881 Husic, A.: Numerical modeling and isotope tracers to investigate karst biogeochemistry and transport
882 processes, 2018.
883 Jin, L., and Brantley, S. L.: Soil chemistry and shale weathering on a hillslope influenced by convergent
884 hydrologic flow regime at the Susquehanna/Shale Hills Critical Zone Observatory, Applied Geochemistry,
885 26, Supplement, S51-S56, http://dx.doi.org/10.1016/j.apgeochem.2011.03.027, 2011.
886 Jin, L. X., Ravella, R., Ketchum, B., Bierman, P. R., Heaney, P., White, T., and Brantley, S. L.: Mineral
887 weathering and elemental transport during hillslope evolution at the Susquehanna/Shale Hills Critical
888 Zone Observatory, Geochim Cosmochim Ac, 74, 3669-3691, 10.1016/j.gca.2010.03.036, 2010.
889 Keune, J., Gasper, F., Goergen, K., Hense, A., Shrestha, P., Sulis, M., and Kollet, S.: Studying the influence
890 of groundwater representations on land surface-atmosphere feedbacks during the European heat wave
891 in 2003, Journal of Geophysical Research: Atmospheres, 121, 13,301-313,325,
892 https://doi.org/10.1002/2016JD025426, 2016.
893 Kirchner, J. W., Hooper, R. P., Kendall, C., Neal, C., and Leavesley, G.: Testing and validating environmental
894 models, Science of the Total Environment, 183, 33-47, 10.1016/0048-9697(95)04971-1, 1996.
895 Kuntz, B. W., Rubin, S., Berkowitz, B., and Singha, K.: Quantifying Solute Transport at the Shale Hills Critical
896 Zone Observatory, Vadose Zone Journal, 10, 843-857, 10.2136/vzj2010.0130, 2011.
897 Leonard, L., and Duffy, C. J.: Essential terrestrial variable data workflows for distributed water resources
898 modeling, Environmental modelling & software, 50, 85-96, 2013.
899 Li, L., Salehikhoo, F., Brantley, S. L., and Heidari, P.: Spatial zonation limits magnesite dissolution in porous
900 media, Geochimica et Cosmochimica Acta, 126, 555-573, 10.1016/j.gca.2013.10.051, 2014.
901 Li, L., Bao, C., Sullivan, P. L., Brantley, S., Shi, Y., and Duffy, C.: Understanding watershed
902 hydrogeochemistry: 2. Synchronized hydrological and geochemical processes drive stream chemostatic
903 behavior, Water Resources Research, 53, 2346-2367, 2017a.

904   Li, L., Maher, K., Navarre-Sitchler, A., Druhan, J., Meile, C., Lawrence, C., Moore, J., Perdrial, J., Sullivan, P.,
905   Thompson, A., Jin, L., Bolton, E. W., Brantley, S. L., Dietrich, W. E., Mayer, K. U., Steefel, C. I., Valocchi, A.,
906   Zachara, J., Kocar, B., McIntosh, J., Tutolo, B. M., Kumar, M., Sonnenthal, E., Bao, C., and Beisman, J.:
907   Expanding the role of reactive transport models in critical zone processes, Earth-Science Reviews, 165,
908   280-301, http://dx.doi.org/10.1016/j.earscirev.2016.09.001, 2017b.
909   Li, L.: Watershed reactive transport, Reviews in Mineralogy and Geochemistry, 85, 381-418, 2019.
910   Li, L., Sullivan, P. L., Benettin, P., Cirpka, O. A., Bishop, K., Brantley, S. L., Knapp, J. L. A., Meerveld, I.,
911   Rinaldo, A., Seibert, J., Wen, H., and Kirchner, J. W.: Toward catchment hydro‐biogeochemical theories,
912   WIREs Water, 10.1002/wat2.1495, 2020.
913   Lin, H.: Temporal stability of soil moisture spatial pattern and subsurface preferential flow pathways in
914   the Shale Hills Catchment, Vadose Zone Journal, 5, 317-340, 2006.
915   Lindström, G., Rosberg, J., and Arheimer, B.: Parameter Precision in the HBV-NP Model and Impacts on
916   Nitrogen Scenario Simulations in the Rönneå River, Southern Sweden, AMBIO: A Journal of the Human
917   Environment, 34, 533-537, 535, 2005.
918   Lindström, G., Pers, C., Rosberg, J., Strömqvist, J., and Arheimer, B.: Development and testing of the HYPE
919   (Hydrological Predictions for the Environment) water quality model for different spatial scales, Hydrology
920   Research, 41, 295-319, 10.2166/nh.2010.007, 2010.
921   Liu, Y., Wang, C., He, N., Wen, X., Gao, Y., Li, S., Niu, S., Butterbach‐Bahl, K., Luo, Y., and Yu, G.: A global
922   synthesis of the rate and temperature sensitivity of soil nitrogen mineralization: latitudinal patterns and
923   mechanisms, Global change biology, 23, 455-464, 2017.
924   Lloyd, J., and Taylor, J. A.: On the Temperature Dependence of Soil Respiration, Functional Ecology, 8, 315-
925   323, 10.2307/2389824, 1994.
926   López, B., Sabaté, S., and Gracia, C.: Vertical distribution of fine root density, length density, area index
927   and mean diameter in a Quercus ilex forest, Tree Physiology, 21, 555-560, 2001.
928   McMurtrie, R. E., Iversen, C. M., Dewar, R. C., Medlyn, B. E., Näsholm, T., Pepper, D. A., and Norby, R. J.:
929   Plant root distributions and nitrogen uptake predicted by a hypothesis of optimal root foraging, Ecology
930   and Evolution, 2, 1235-1250, 2012.
931   Miller, M. P., Tesoriero, A. J., Hood, K., Terziotti, S., and Wolock, D. M.: Estimating Discharge and Nonpoint
932   Source Nitrate Loading to Streams From Three End-Member Pathways Using High-Frequency Water
933   Quality Data, Water Resources Research, 53, 10201-10216, 10.1002/2017wr021654, 2017.
934   Miller, M. P., Capel, P. D., García, A. M., and Ator, S. W.: Response of Nitrogen Loading to the Chesapeake
935   Bay to Source Reduction and Land Use Change Scenarios: A SPARROW‐Informed Analysis, JAWRA
936   Journal of the American Water Resources Association, 56, 100-112, 2020.
937   Moatar, F., Abbott, B. W., Minaudo, C., Curie, F., and Pinay, G.: Elemental properties, hydrology, and
938   biology interact to shape concentration‐discharge curves for carbon, nutrients, sediment, and major
939   ions, Water Resources Research, 53, 1270-1287, 2017.
940   Moriasi, D. N., Arnold, J. G., Van Liew, M. W., Bingner, R. L., Harmel, R. D., and Veith, T. L.: Model evaluation
941   guidelines for systematic quantification of accuracy in watershed simulations, T Asabe, 50, 885-900, 2007.
942   Moriasi, D. N., Gitau, M. W., Pai, N., and Daggupati, P.: Hydrologic and water quality models: Performance
943   measures and evaluation criteria, T Asabe, 58, 1763-1785, 2015.
944   Musolff, A., Schmidt, C., Selle, B., and Fleckenstein, J. H.: Catchment controls on solute export, Adv. Water
945   Resour., 86, 133-146, 10.1016/j.advwatres.2015.09.026, 2015.
946   Neitsch, S. L., Arnold, J. G., Kiniry, J. R., and Williams, J. R.: Soil and water assessment tool theoretical
947   documentation version 2009, Texas Water Resources Institute, 2011.
948   Porporato, A., D'odorico, P., Laio, F., and Rodriguez-Iturbe, I.: Hydrologic controls on soil carbon and
949   nitrogen cycles. I. Modeling scheme, Advances in water resources, 26, 45-58, 2003.
950   Qu, Y., and Duffy, C. J.: A semidiscrete finite volume formulation for multiprocess watershed simulation,
951   Water Resources Research, 43, W08419, 2007.

952 Regnier, P., and Steefel, C. I.: A high resolution estimate of the inorganic nitrogen flux from the Scheldt
953 estuary to the coastal North Sea during a nitrogen-limited algal bloom, spring 1995, Geochimica et
954 Cosmochimica Acta, 63, 1359-1374, 10.1016/s0016-7037(99)00034-4, 1999.
955 Rutherford, D. W., Chiou, C. T., and Kile, D. E.: Influence of soil organic matter composition on the partition
956 of organic compounds, Environmental science & technology, 26, 336-340, 1992.
957 Saad, Y., and Schultz, M. H.: GMRES: A generalized minimal residual algorithm for solving nonsymmetric
958 linear systems, SIAM Journal on scientific and statistical computing, 7, 856-869, 1986.
959 Saberi, L., Crystal Ng, G. H., Nelson, L., Zhi, W., Li, L., La Frenierre, J., and Johnstone, M.: Spatiotemporal
960 Drivers of Hydrochemical Variability in a Tropical Glacierized Watershed in the Andes, Water Resources
961 Research, 57, e2020WR028722, 2021.
962 Scudeler, C., Pangle, L., Pasetto, D., Niu, G.-Y., Volkmann, T., Paniconi, C., Putti, M., and Troch, P.:
963 Multiresponse modeling of variably saturated flow and isotope tracer transport for a hillslope experiment
964 at the Landscape Evolution Observatory, Hydrology and Earth System Sciences, 20, 4061-4078, 2016.
965 Sebestyen, S. D., Ross, D. S., Shanley, J. B., Elliott, E. M., Kendall, C., Campbell, J. L., Dail, D. B., Fernandez,
966 I. J., Goodale, C. L., and Lawrence, G. B.: Unprocessed Atmospheric Nitrate in Waters of the Northern
967 Forest Region in the US and Canada, Environmental science & technology, 53, 3620-3633, 2019.
968 Seibert, J., Grabs, T., Köhler, S., Laudon, H., Winterdahl, M., and Bishop, K.: Linking soil- and stream-water
969 chemistry based on a Riparian Flow-Concentration Integration Model, Hydrol. Earth Syst. Sci., 13, 2287-
970 2297, 10.5194/hess-13-2287-2009, 2009.
971 Shi, Y.: Development of a land surface hydrologic modeling and data assimilation system for the study of
972 subsurface-land surface interaction, 2012.
973 Shi, Y., Davis, K. J., Duffy, C. J., and Yu, X.: Development of a coupled land surface hydrologic model and
974 evaluation at a critical zone observatory, Journal of Hydrometeorology, 14, 1401-1420, 2013.
975 Skamarock, W., and Klemp, J.: A Description of the Advanced Research WRF Model Version 4. Ncar
976 Technical Notes, No, NCAR/TN-556+ STR, 2019.
977 Steefel, C., Appelo, C., Arora, B., Jacques, D., Kalbacher, T., Kolditz, O., Lagneau, V., Lichtner, P., Mayer, K.
978 U., and Meeussen, J.: Reactive transport codes for subsurface environmental simulation, Computational
979 Geosciences, 19, 445-478, 2015.
980 Steefel, C. I., and Lasaga, A. C.: A coupled model for transport of multiple chemical species and kinetic
981 precipitation/dissolution reactions with application to reactive flow in single phase hydrothermal systems,
982 American Journal of science, 294, 529-592, 1994.
983 Sullivan, P. L., Hynek, S. A., Gu, X., Singha, K., White, T., West, N., Kim, H., Clarke, B., Kirby, E., Duffy, C.,
984 and Brantley, S. L.: Oxidative dissolution under the channel leads geomorphological evolution at the Shale
985 Hills catchment, American Journal of Science, 316, 981-1026, 10.2475/10.2016.02, 2016.
986 Taylor, R. G., Scanlon, B., Döll, P., Rodell, M., Van Beek, R., Wada, Y., Longuevergne, L., Leblanc, M.,
987 Famiglietti, J. S., and Edmunds, M.: Ground water and climate change, Nature climate change, 3, 322,
988 2013.
989 van der Velde, Y., de Rooij, G. H., Rozemeijer, J. C., van Geer, F. C., and Broers, H. P.: Nitrate response of
990 a lowland catchment: On the relation between stream concentration and travel time distribution
991 dynamics, Water Resources Research, 46, 10.1029/2010wr009105, 2010.
992 van der Velde, Y., Vercauteren, N., Jaramillo, F., Dekker, S. C., Destouni, G., and Lyon, S. W.: Exploring
993 hydroclimatic change disparity via the Budyko framework, Hydrological Processes, 28, 4110-4118,
994 10.1002/hyp.9949, 2014.
995 Weiler, M., and McDonnell, J. R. J.: Testing nutrient flushing hypotheses at the hillslope scale: A virtual
996 experiment approach, J. Hydrol., 319, 339-356, 10.1016/j.jhydrol.2005.06.040, 2006.
997 Weitzman, J. N., and Kaye, J. P.: Nitrogen Budget and Topographic Controls on Nitrous Oxide in a Shale‐
998 Based Watershed, Journal of Geophysical Research: Biogeosciences, 123, 1888-1908, 2018.

999 Wen, H., and Li, L.: An upscaled rate law for magnesite dissolution in heterogeneous porous media,
1000 Geochimica et Cosmochimica Acta, 210, 289-305, 2017.
1001 Wen, H., and Li, L.: An upscaled rate law for mineral dissolution in heterogeneous media: The role of time
1002 and length scales, Geochimica et Cosmochimica Acta, 235, 1-20, 2018.
1003 Wen, H., Perdrial, J., Bernal, S., Abbott, B. W., Dupas, R., Godsey, S. E., Harpold, A., Rizzo, D., Underwood,
1004 K., and Adler, T.: Temperature controls production but hydrology controls export of dissolved organic
1005 carbon at the catchment scale, 24, 945-966, 2020.
1006 Wen, H., Brantley, S. L., Davis, K. J., Duncan, J. M., and Li, L.: The Limits of Homogenization: What
1007 Hydrological Dynamics can a Simple Model Represent at the Catchment Scale?, Water Resources
1008 Research, 57, e2020WR029528, https://doi.org/10.1029/2020WR029528, 2021.
1009 Wolery, T. J.: EQ3/6, a software package for geochemical modeling of aqueous systems: package overview
1010 and installation guide (version 7.0), 1992.
1011 Xiao, D., Shi, Y., Brantley, S. L., Forsythe, B., DiBiase, R., Davis, K., and Li, L.: Streamflow Generation From
1012 Catchments of Contrasting Lithologies: The Role of Soil Properties, Topography, and Catchment Size,
1013 Water Resources Research, n/a, 10.1029/2018wr023736, 2019.
1014 Xiao, D., Brantley, S. L., and Li, L.: Vertical Connectivity Regulates Water Transit Time and Chemical
1015 Weathering at the Hillslope Scale, Water Resources Research, 57, e2020WR029207,
1016 https://doi.org/10.1029/2020WR029207, 2021.
1017 Yan, Q., Duan, Z., Mao, J., Li, X., and Dong, F.: Effects of root-zone temperature and N, P, and K supplies
1018 on nutrient uptake of cucumber (Cucumis sativus L.) seedlings in hydroponics, Soil Science and Plant
1019 Nutrition, 58, 707-717, 2012.
1020 Yan, Z., Bond-Lamberty, B., Todd-Brown, K. E., Bailey, V. L., Li, S., Liu, C., and Liu, C.: A moisture function
1021 of soil heterotrophic respiration that incorporates microscale processes, Nat Commun, 9, 2562,
1022 10.1038/s41467-018-04971-6, 2018.
1023 Zarnetske, J. P., Bouda, M., Abbott, B. W., Saiers, J., and Raymond, P. A.: Generality of hydrologic transport
1024 limitation of watershed organic carbon flux across ecoregions of the United States, Geophysical Research
1025 Letters, 45, 11,702-711,711, 2018.
1026 Zhi, W., Li, L., Dong, W., Brown, W., Kaye, J., Steefel, C., and Williams, K. H.: Distinct Source Water
1027 Chemistry Shapes Contrasting Concentration-Discharge Patterns, Water Resour. Res., 55, 4233-4251,
1028 10.1029/2018wr024257, 2019.
1029 Zhi, W., and Li, L.: The Shallow and Deep Hypothesis: Subsurface Vertical Chemical Contrasts Shape Nitrate
1030 Export Patterns from Different Land Uses, Environmental Science & Technology, 54, 11915-11928,
1031 10.1021/acs.est.0c01340, 2020.
1032 Zhou, T., Shi, P., Hui, D., and Luo, Y.: Global pattern of temperature sensitivity of soil heterotrophic
1033 respiration (Q10) and its implications for carbon‐climate feedback, Journal of Geophysical Research:
1034 Biogeosciences, 114, 2009.

1035

1036

1037